Discovery of lipid binding sites in a ligand-gated ion channel by integrating simulations and cryo-EM

Cathrine Bergh[1], Urška Rovšnik[2], Rebecca J. Howard[2], and Erik Lindahl[1,2,†]

[1]Science for Life Laboratory & Swedish e-Science Research Center, Department of Applied Physics, KTH Royal Institute of Technology, Solna, Sweden
[2]Science for Life Laboratory, Department of Biochemistry and Biophysics, Stockholm University, Solna, Sweden
[†]Corresponding author: erik.lindahl@scilifelab.se

Abstract

Ligand-gated ion channels transduce electrochemical signals in neurons and other excitable cells. Aside from canonical ligands, phospholipids are thought to bind specifically to the transmembrane domain of several ion channels. However, structural details of such lipid contacts remain elusive, partly due to limited resolution of these regions in experimental structures. Here, we discovered multiple lipid interactions in the channel GLIC by integrating cryo-electron microscopy and large-scale molecular simulations. We identified 25 bound lipids in the GLIC closed state, a conformation where none, to our knowledge, were previously known. Three lipids were associated with each subunit in the inner leaflet, including a buried interaction disrupted in mutant simulations. In the outer leaflet, two intrasubunit sites were evident in both closed and open states, while a putative intersubunit site was preferred in open-state simulations. This work offers molecular details of GLIC-lipid contacts particularly in the ill-characterized closed state, testable hypotheses for state-dependent binding, and a multidisciplinary strategy for modeling protein-lipid interactions.

Introduction

Pentameric ligand-gated ion channels (pLGICs) can be found in numerous cell types, particularly in the postsynaptic membrane of the vertebrate nervous system, where they transduce electrochemical signals upon neurotransmitter binding [1]. Gating in pLGICs is initiated by ligand binding in the extracellular domain (ECD), which is believed to lead to large twisting and blooming motions in the ECD, followed by rearrangements in the transmembrane domain (TMD), which eventually lead to opening of the central transmembrane pore. In addition to soluble ligands and numerous allosteric modulators, lipid components of the plasma membrane have been shown to bind to a variety of membrane proteins, potentially modifying their stability or gating [2]. For pLGICs, lipid composition was shown to influence reconstitution of functional activity in the *Torpedo* nicotinic acetylcholine receptor (nAChR) as early as the 1980s [3–6]. Multiple members of the pLGIC family, particularly nAChRs and prokaryotic channels cloned from *Gloeobacter violaceus* (GLIC) and *Dickeya dadantii* (formerly *Erwinia chrysanthemi*, reflected in the channel name ELIC), have since demonstrated functional sensitivity or co-purification with membrane lipids [7]. It has been suggested that lipids interact with membrane-facing loops from the ECD, or with the four membrane-spanning helices (M1–M4) of the TMD. However, many structural details of these lipid interactions remain poorly understood [8].

A critical challenge to elucidating lipid-protein interactions is their typically poor definition in experimental densities. Among more than 100 deposited structures in the protein data bank for GLIC crystallized under activating conditions, several lipid poses have been reported [9–15]. These include an outer-leaflet site on the complementary face of a single GLIC subunit, an inner-leaflet site on the principal face of a subunit, and an interfacial inner-leaflet site making contacts with two neighboring subunits [7]. In one case, an additional outer-leaflet density was built as a detergent molecule [16]. However, the positions and orientations

of these membrane components or mimetics vary between structures, and typically include only a subset of their constituent atoms.

Another issue is the potential dependence of lipid interactions on the functional state of the membrane protein. In most members of the pLGIC family, binding of a chemical stimulus to the ECD favors a transition from an unliganded, nonconducting state to a liganded, conducting state, and in some cases to a subsequent liganded, desensitized state. Although terminology in the field may vary, conditions predicted to favor the first versus second of these states are referred to here as *resting* versus *activating*; the corresponding conformations of the TMD pore are designated *closed* versus *open*. No lipids were reported with the lone X-ray structure of GLIC under resting conditions, raising the possibility that interactions could be state-dependent, or obscured by the relatively low overall resolution of this dataset (4.0 Å) [17]. Independent validation of phospholipid interactions in the closed as well as open states of GLIC would provide a valuable baseline for investigating such contacts in the larger family of pLGICs, including pharmacologically important effects of components such as cholesterol and neurosteroids that modulate LGICs [7, 18].

Molecular dynamics simulations offer an alternative approach to visualizing lipid-protein interactions. All-atom simulations of membrane proteins typically involve solvating an experimental structure in a simplified lipid bilayer as well as water and ions, all of which move freely according to physical principles encoded in the force field. Simulations on both atomistic and coarse-grained levels have recently enabled the identification of specific lipid interactions in pLGICs such as ELIC [19, 20], nAChRs [21], glycine [22] and serotonin-3 receptors [23], but were typically limited to shorter timescales or specific protein conformations. We recently reported free-energy landscapes for GLIC gating using Markov state modeling of 120 µs unrestrained molecular dynamics simulations [24]. Because GLIC is activated by external acidification (pH < 6), resting versus activating conditions could be approximated throughout these simulations by setting titratable amino-acid residues as deprotonated versus protonated, respectively. Under these two conditions, different distributions of functional states were captured, consistent with the relative stabilization of open versus closed channels upon activation. Although our previous analyses focused on conformational changes of the protein alone, the same simulation data encodes a wealth of additional features, including membrane lipids. We also recently reported the first structural data for GLIC using cryogenic electron microscopy (cryo-EM), which enabled the reconstruction of multiple new closed structures [25].

Here, we present the first cryo-EM structure of GLIC in a closed conformation with multiple bound lipids resolved in each subunit. These were built into non-protein densities evident in the cryo-EM data, further informed by closed-state lipid occupancies independently identified and characterized from extensive molecular dynamics simulations. Five distinct closed-state lipid-interaction sites per subunit covered intra- and intersubunit cavities in the inner and outer leaflets. We also compared open-state lipid occupancies from our simulations with previous open X-ray structures, identifying six possible poses. These analyses allowed us to predict novel features of lipid interactions in GLIC, including a potentially state-dependent binding site at the outer subunit interface, and a potential role for lipid-tail saturation in binding at the inner leaflet, further validated through mutant simulations. In addition to casting light on selective lipid interactions with LGICs, this work demonstrates the combined power of experimental densities and molecular simulations to support the characterization of lipid binding sites in systems challenged by heterogeneous or otherwise low-resolution data.

Results

Markov state modeling and cryo-EM data resolve lipid-protein interactions

We previously reported cryo-EM structures of GLIC in multiple closed states [26], and demonstrated how Markov state modeling (MSM) can predict shifts in the GLIC gating landscape under resting versus activating conditions [24]. In this work we have combined new cryo-EM reconstructions with simulations newly extended to achieve better sampling of lipids, which made it possible to identify five previously uncharacterized lipid poses interacting with each subunit in the closed state of GLIC (Fig. 1A).

In our computational work, we used molecular simulations of GLIC conducted under either resting or activating conditions [24] to quantify occupancy and duration of lipid interactions. Simulation frames previously identified as either closed or open (Fig. 1B) were clustered to their corresponding state, and used to generate densities occupied by lipids that contacted the protein in at least 40% of simulation frames

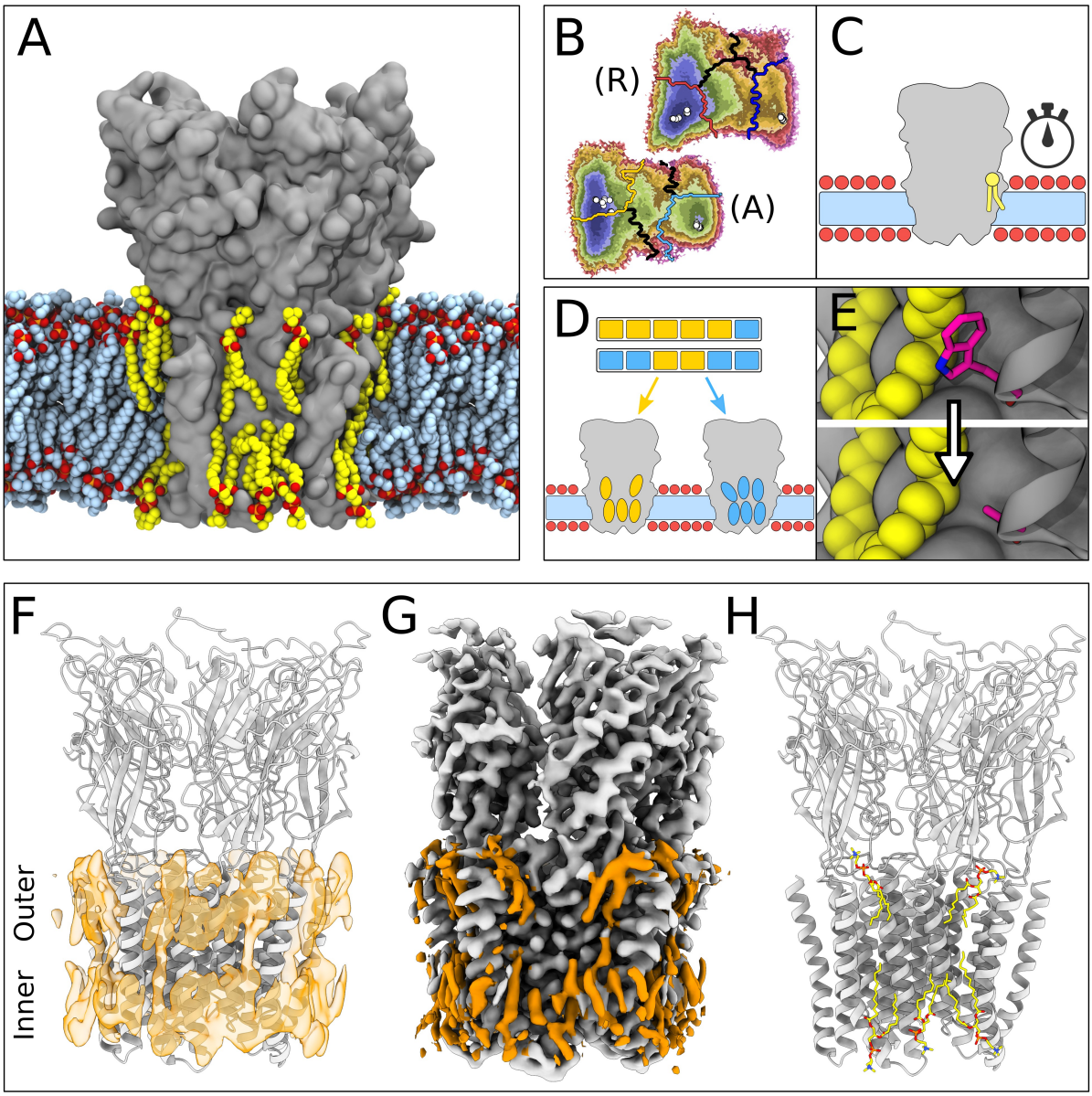

Figure 1: Lipid-protein interactions mapped by Markov state modeling and cryo-electron microscopy. (A) GLIC structure (gray) embedded in a lipid bilayer (blue) with interacting lipids highlighted (yellow). (B) Markov state models were used to cluster simulations conducted under resting (R) or activating (A) conditions into five states, including closed (orange outline) and open (blue outline), with experimental structures plotted in white. (C) The duration of lipid interactions were measured in individual trajectories. (D) From clustered trajectory frames, lipid-occupied densities were obtained for closed (orange) and open (blue) states. (E) Further simulations were performed to test the role of residues involved in extensive lipid interactions. (F) View of a manually built cryo-EM model of closed GLIC (gray) with computationally derived lipid occupancies in orange (semi-transparent). (G) Cryo-EM reconstruction of closed GLIC (gray), with partly defined non-protein densities (orange). (H) Equivalent view of a manually built cryo-EM model as in F, with newly built lipids shown as sticks (yellow, heteroatom; phosphorus, orange; oxygen, red; nitrogen, blue).

(Fig. 1D,F). In order to distinguish presumed functional endpoints, snapshots classified into macrostates other than closed or open (Fig, 1B, colored boundaries) were excluded from occupancy calculations, except as indicated below. In parallel, mean duration times of lipid contacts were quantified for each amino acid residue in each 1.7 µs trajectory (50 seeds $\times 2$ conditions $\times 5$ subunits = 500 trajectories; Fig. 1C). In some cases, we validated notable contacts by additional simulations in the presence of targeted mutations (Fig. 1E).

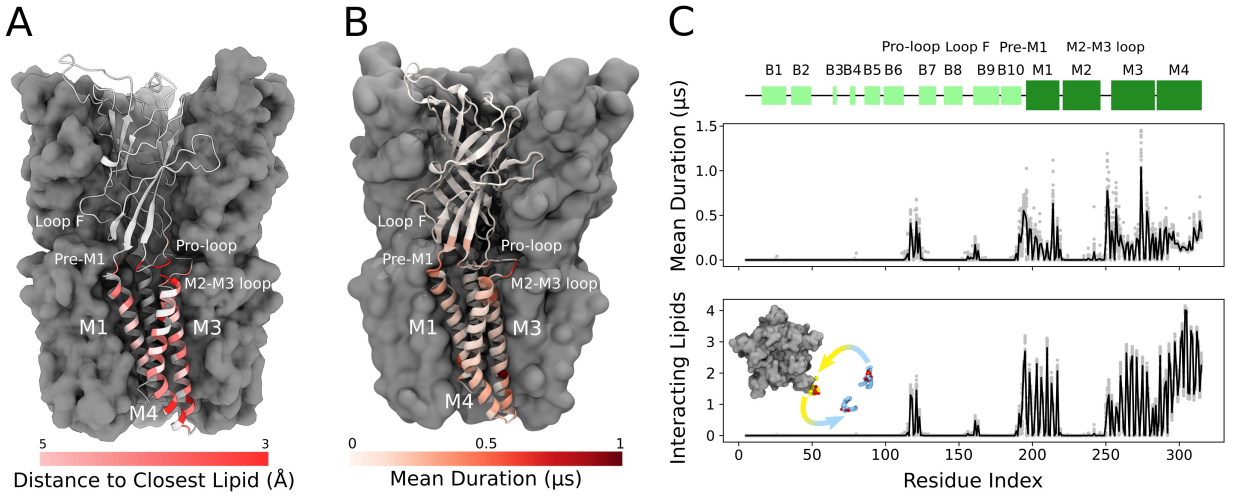

Figure 2: Cryo-EM and simulations reveal lipid interaction sites. (A) Cryo-EM reconstruction of closed GLIC with distance to the interacting lipids colored according to the bar below. (B) Mean duration time of lipid-residue interactions, scaled (white–red) according the the color bar below, projected onto the closed-state GLIC structure (PDB ID: 4NPQ). For both panels, a single subunit is displayed in cartoon. (C) Secondary structure schematic for GLIC (top), mean duration time of each lipid-residue interaction (middle), and number of lipids interacting with each residue during simulations (bottom).

In our cryo-EM work, a new GLIC reconstruction was generated by merging datasets previously collected under multiple pH conditions [26]. The predominant class corresponded to an apparently closed channel at an overall resolution of 2.9 Å, the highest resolution yet reported for GLIC in this state (Supplementary Fig. S1, Table 1). After building all residues, additional non-protein densities were evident in both the outer and inner leaflets of the predicted membrane region. These were further sharpened by post-processing with ResolveCryoEM [27] and LocScale [28]. From the combined observations of these cryo-EM densities (Fig. 1G) and occupied densities in closed-state simulations (Fig. 1F), five lipids were built in association with each of the five GLIC subunits, for a total of 25 lipid molecules (Fig. 1H).

Lipids built in this structure formed close contacts with GLIC residues in several membrane-proximal regions. These included an ECD motif with a characteristic proline/cysteine-rich turn, known as the Pro-loop (or Cys-loop in eukaryotes); N-terminal residues of the M1 helix; regions in and surrounding the M2–M3 loop; interfacial residues at the C-terminal end of M3; and inward- and outward-facing regions of M4 (Fig. 2A). In several cases, these regions corresponded to longer-duration lipid interactions in molecular simulations (Fig. 2B,C). In the inner leaflet, relatively long-lasting interactions were found at the subunit interface, involving buried residues in both the M1 and M3 helices. In the outer leaflet, longer interactions were focused around the pre-M1 and M2-M3 loops. Although lateral lipid diffusion was expected to be slow relative to the timescales of each trajectory (1.7 µs), we found residues throughout M1, M3 and M4 that exchanged contacts with 2–4 different lipid molecules in individual simulations (Fig. 2C). Such exchange events suggest that the durations of lipid contacts observed in this work can be at least partly attributed to interaction stabilities, not solely to sampling limitations.

Protein and lipid determinants of state-independent inner-leaflet binding

Because transverse lipid exchange is far slower than the timescale of our simulations, we focused analyses on each membrane leaflet separately. In the inner leaflet, occupied densities from closed-state simulation snapshots were largely superimposable with those from open snapshots (Fig. 3A), indicating lipid interactions in this region were not notably state-dependent. In both states, three types of inner-leaflet computational densities could be observed; accordingly, our cryo-EM reconstruction included three types of forked densities, which could be built as three independent lipids per subunit (Fig. 3B). One density spanned the principal M3 and complementary M1 helices of neighboring subunits; one was located between M3 and M4 on the principal face of each subunit; and another spanned M1 and M4 on the complementary face of each subunit. Interfacial and principal-face inner-leaflet lipids have been resolved in previous open-state X-ray structures

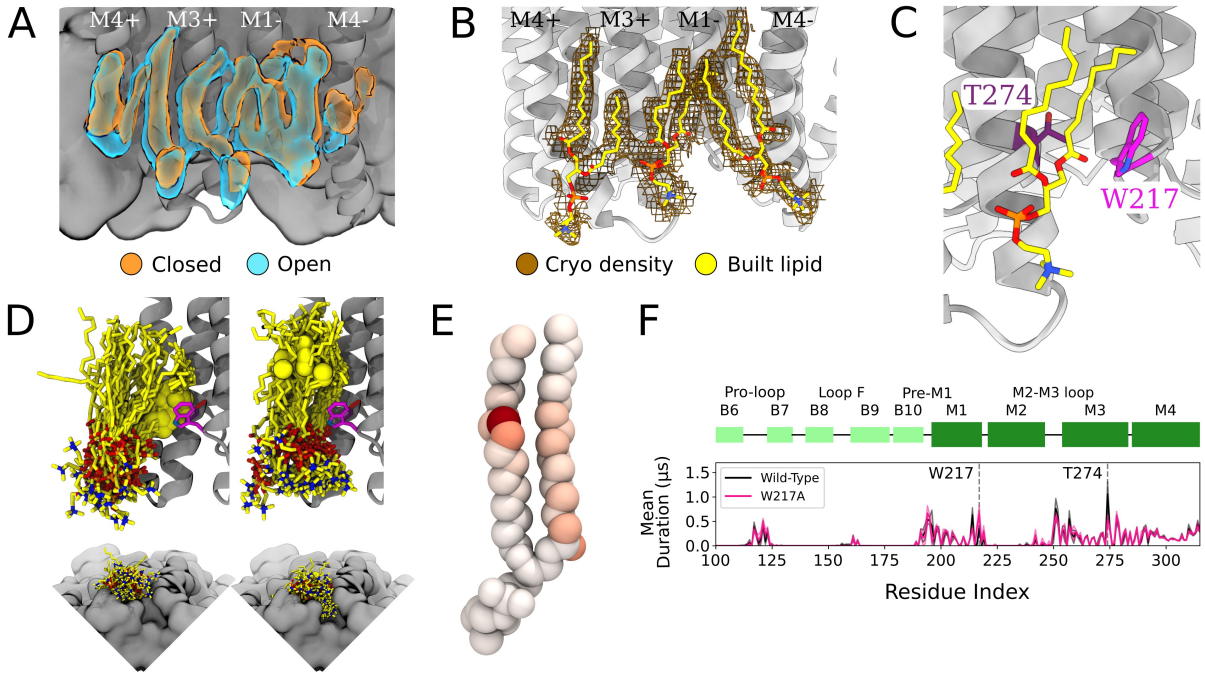

Figure 3: Protein and lipid determinants of state-independent inner-leaflet binding. (A) Computationally-derived densities from the open (blue) and closed (orange) states generally agree. (B) Modeled lower leaflet lipids (yellow, stick, heteroatom coloring) from cryo-EM densities (brown mesh). (C) Zoom-in view of the lower leaflet buried lipid interaction site at the M1-M3 subunit interface. Lipids particularly interact with residues T274 (purple) and W217 (magenta). (D) The 100 simulation frames that best fit the computational densities could be clustered into two distinct binding poses at the T274 binding site. When the tail with a double-bond was in the pocket (left) lipid heads are directed out from the channel, while it samples a larger variety of poses when the lipid tail without a double-bond is in the pocket (right), with possibility of the head to enter into a crevice on the bottom of the channel, approaching the pore. The M4 helix is not shown for clarity in the top panels. (E) Number of contacts made by specific POPC lipid atoms with residue T274 in simulations at both resting and activating conditions (red indicate high numbers and white low). For the tail with a double-bond the interactions are concentrated around the double-bond region while for the tail without a double-bond interactions are interspersed along the tail. (F) Mutation of residue W217 lining this pocket, reveals shortened interactions for an alanine mutation (magenta).

of GLIC [29] as well as other pLGIC structures [7], while the complementary inner-leaflet GLIC site, to our knowledge, has not been reported before.

The lipid occupying the subunit interface accounted for some of the longest-lived interactions in the simulations, both with M1 and M3 (Fig. 3C,F). A particularly frequent contact at this site in our simulations was the unsaturated C=C bond of 1-palmitoyl-2-oleoyl-sn-glycero-3-phosphocholine (POPC) (Fig. 3D,E). Interestingly, lipids adopted two types of poses in this site, depending on the placement of the unsaturated tail. The double bond was frequently wedged between M3-T274 and M1-W217 at the intersubunit cleft, with the remainder of the lipid projecting out towards the membrane (Fig. 3D, left). When the double bond exited the pocket, the more flexible saturated tail was able to enter the intersubunit cleft and sample a range of poses characterized by contacts distributed more broadly across the lipid tail (Fig. 3E), and resulting in some deeply buried poses (Fig. 3D, right).

To further explore the influence of specific amino acid contacts on this interfacial lipid pose, we performed additional MD simulations with mutations in targeted sites. Interestingly, the buried M3 position 274 remained the contact of longest duration, even when mutated from threonine to a smaller (alanine) or larger (tryptophan) residue (Supplementary Fig. S2). Conversely, removing the bulky tryptophan sidechain at position 217 (W217A) dramatically shortened lipid contacts at the more deeply buried T274 (Fig. 3F). These results confirm the importance of specific sidechain identities on the protein surface (W217) in influencing lipid binding pose, whereas even long-lived contacts (T274) may be sustained more by their buried position than side chain size.

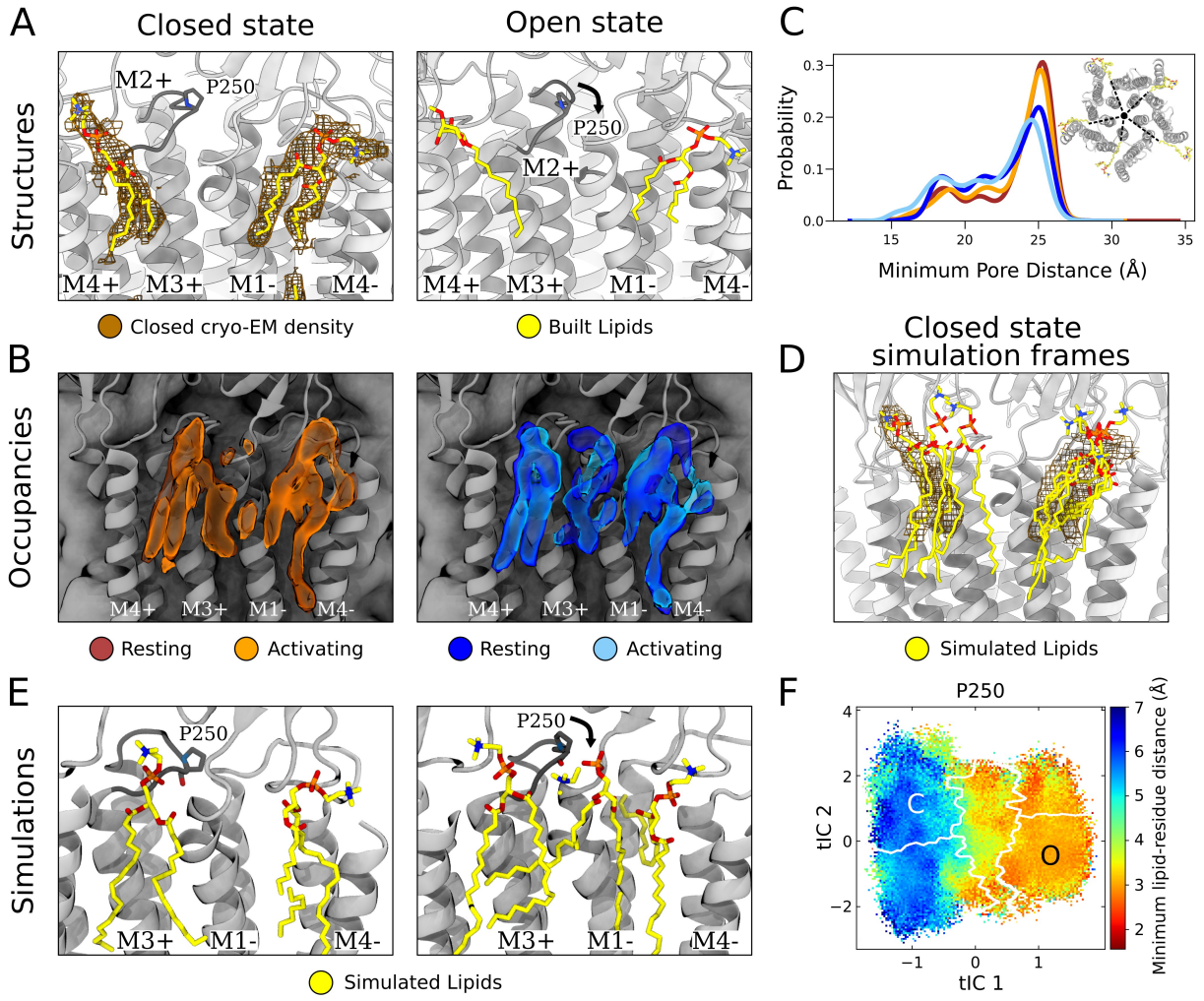

Figure 4: State-dependent protein-lipid interactions in the upper leaflet. (A) Zoom view of the outer transmembrane domain of the closed GLIC cryo-EM structure (left, gray), showing non-protein cryo-EM densities (brown mesh) overlaid with built lipids (yellow). For comparison, the same region is shown of an open state x-ray structure (PDB ID: 6HZW) [16] with built lipid and detergent in equivalent positions (right). Conformational changes of the M2-M3 loop, including residue P250, in channel opening are highlighted. Lipids are colored by heteroatom (phosphorus, orange; oxygen, red; nitrogen, blue). (B) Same region as in (A) showing densities occupied by lipids ($\geq$40%) in simulation frames clustered as closed (left, orange) or open (right, blue) states (top). Open-state differences include an enhanced density on the right-hand side of the intersubunit cleft, and a more deeply penetrating density in the intrasubunit cleft. Overlaid densities represent simulations conducted under resting (dark shades) or activating (light shades) conditions, which were largely superimposable within each state. (C) Radial distribution of the lipid atoms closest to the upper pore, showing closer association of lipids in the open (light blue, dark blue) versus closed (orange, red) states. (D) Same region and cryo-EM densities (mesh) as in (A) overlaid with lipids from a few simulation frames where the lipids had the highest correlation with the closed state computational occupancies in (B). (E) Snapshots from simulation frames that had the highest correlation with the occupancies (activating conditions) in (B). The open states are characterized by an additional lipid at the intersubunit site, interacting with the oxygen of P250. (F) The minimum distance between P250 and the closest lipid projected onto the free energy landscapes obtained from Markov state modeling. P250-lipid interactions are possible in the open state, but not in the closed state.

Intrasubunit lipids and state dependence in the outer leaflet

In the outer leaflet, closed-state cryo-EM densities enabled confident building of two lipid poses, associated with either the principal or complementary face of each subunit (Fig. 4A, left). Lipids have previously been resolved in open and inhibited X-ray structures of GLIC at a complementary-face outer-leaflet site between the M1 and M4 helices [16, 29–31] (Fig. 4A, right), comparable to that observed here in the cryo-EM closed state. To our knowledge no lipid has been reported at any other outer-leaflet site in GLIC, though

a principal-face density was built as a detergent molecule in at least one open-state X-ray structure [16] (Fig. 4A, right).

In closed-state simulation snapshots, outer-leaflet densities largely corresponded to our closed-state cryo-EM data, including distinct interaction sites on the complementary and principal faces (Fig. 4B, left). In these and other sites, occupancies and distributions were largely superimposable when calculated from Markov state models constructed independently under resting versus activating conditions (Fig. 4B,C), indicating the reproducibility of the approach and relative insensitivity of the lipid-interaction landscape to pH. However, comparing open- versus closed-state occupancies suggested state-dependent differences in lipid interactions, as described below (Fig. 4B).

At the complementary face, lipid tails were more likely to enter a buried region of the intrasubunit pocket in the open state. Although the difference was subtle, the distribution of outer-leaflet lipids shifted in snapshots of open compared to closed conformations, increasing (5% to 10%) the probability of lipids penetrating 18 Å from the pore axis (Fig. 4C). Interestingly, lipid tails entered even deeper (15 Å from the pore) in an alternative state within the GLIC gating landscape (Fig. S3A), previously associated with channel desensitization due to relative contraction at the intracellular gate (Fig. S3B) [24]. Although the lipid tails were too poorly resolved in our structural data to definitively capture buried interactions at the complementary site, it is interesting that the simulations implicated them in channel opening (and possibly in transitions further along the activation pathway) given that the deeper parts of this site have been shown to bind allosteric modulators such as propofol [32].

At the principal face, interactions with lipid heads were more diverse than those with lipid tails. In our closed cryo-EM and a previously reported open X-ray structure [16], the lipid or detergent head in this site tilted away from the pore axis, towards M4 (Fig. 4A). On initial inspection, lipid-head densities appeared less tilted in closed- versus open-state simulation frames (Fig. S3C). However, lipid heads in this site were relatively flexible, and did align with cryo-EM densities in several closed-state snapshots (Fig. 4D). In fact, lowering the occupancy threshold threshold (from 40% to 30%) revealed an alternative head-group density, tilted towards M4 and covering most of the lipid built in our cryo-EM structure (Fig. S3D). Thus, despite an apparent discrepancy between highly populated densities in simulations and cryo-EM data, both methods supported at least partial occupancy in the built pose. Although this lipid head was primarily associated with M3–M4 on the principal face of one subunit, it also made contacts with residues on the complementary M1 helix (Q193, S196) in closed- but not open-state simulation frames (Supplementary Fig. S3E,F), likely associated with conformational changes during gating.

In addition to the intrasubunit sites described above, a third outer-leaflet lipid density was observed in open-state simulation frames, wedged between two subunits (Fig. 4B, right). This intersubunit pose was not apparent in closed-state simulations (Fig. 4B, left), nor in closed or open experimental GLIC structures (Fig. 4A). The lipid head made particularly close contacts with residue P250 on the M2-M3 loop, which undergoes substantial conformational change away from the pore upon channel opening, along with outer-leaflet regions of M1–M3 (Fig. 4E, Supplementary Fig. S3E,F). These conformational changes were accompanied by a flip of M1 residue F195, which blocked the site in the closed state, but rotated inward to allow closer lipid interactions in the open state (Supplementary Fig. S3F). Indeed, P250 was predominantly located within 3 Å of the nearest lipid atom in open- but not closed-state frames (Fig. 4F). Despite being restricted to the open state, interactions with P250 were among the longest duration in all simulations (Fig. 2C).

Discussion

Lipid interactions have increasingly been shown to play important roles in stabilizing and regulating membrane proteins [33, 34]. Particularly since the emergence of cryo-EM, a growing number of ion channel structures have been reported with detergents or lipids in membrane-facing regions [7, 35]. However, the resolution of bound lipids is typically low compared to the protein, making it challenging to define precise poses or interactions. As a result, lipids and detergents are often built with truncated heads, modeled as isolated hydrocarbon chains, or disregarded altogether to avoid overfitting. Here, we buttressed the building of lipids in the closed state of GLIC by comparing non-protein densities in a relatively high-resolution cryo-EM map with lipid interactions sampled in molecular dynamics simulations.

Our 2.9-Å cryo-EM structure represents, to our knowledge, the highest-resolution closed state of wild-

type GLIC yet reported, and the first in which lipids could be confidently built. Notably, the GLIC sample was solubilized in detergent, which is typically thought to replace biological lipids. Nonetheless, the forked shape of non-protein densities associated with each channel subunit indicated the presence of phospholipids, evidently bound tightly enough to resist substitution by detergent. Similarly persistent lipids have been reported in at least three sites per subunit of open-state GLIC; here, we find evidence for five lipids per subunit in the closed state (Fig. 5A). Continued improvements in membrane-protein cryo-EM may reveal the full extent of persistent lipid binding at key transmembrane sites in the larger pLGIC family.

Molecular dynamics simulations have recently been used to identify lipid binding sites corresponding to experimental data for both prokaryotic and eukaryotic ligand-gated ion channels [19, 20], nAChRs [21], glycine [22] and serotonin-3 receptors [23]. In most cases, the slow rate of lateral lipid diffusion has caused researchers to prefer the use of coarse-grained force fields able to sample longer timescales, but that may overestimate interactions [36]. In addition, such studies typically apply harmonic restraints to the protein, potentially obscuring contributions of protein dynamics to lipid interactions. Indeed, the unrestrained atomistic MD simulations studied here were not expected to capture the maximal duration of stable contacts, as indicated by several interaction times approaching the full 1.7-µsecond trajectory (Fig. 2). Still, they were sufficient to sample exchange of up to four lipids, particularly around the M4 helix. Sampling was further simplified by performing simulations in a uniform POPC membrane, an approximation considered reasonable given the relative insensitivity of GLIC to lipid composition [37]), and that alternative molecular identities of bound lipids could not be precisely determined from structural data. Moreover, by analyzing a large number of parallel trajectories (500 instances of each subunit), we could apply statistics to identify both long-lasting and highly occupied sites. Simulation frames could further be classified with closed or open states by projection onto a previously published Markov state model of GLIC gating, which had been validated against electrophysiology recordings and structural features [24]. In particular since the simulations were initiated by placing the GLIC structures in generated POPC bilayers, it is reassuring that lipid binding sites identified in simulations appear to correspond closely to densities representing lipids bound tightly enough in the cryo-EM data to be retained during reconstitution. The resulting occupancy plots enabled confident distinction between functional annotations, while preserving the protein's flexibility and capacity to transition between states throughout the simulations.

The three lipids identified in the inner leaflet may play primarily structural roles, as they did not vary substantially between closed and open states (Fig. 5). Principal-face and intersubunit sites in our closed cryo-EM structure were largely superimposable with those in open X-ray structures, and all three sites contained comparable densities in closed- and open-state simulation frames. A particularly stable contact in this leaflet featured deep intercalation of a lipid tail between channel subunits, as represented by lipid interactions persisting over 1 µs at residue T274, the longest-lasting in the entire protein (Fig. 2). A lipid in this site was also reported in previous open-state X-ray structures of GLIC [16, 29]. Removal of the sidechain at W217 substantially abbreviated interactions with its buried neighbor T274 (Fig. 3), suggesting this hydrophobic contact helps to stabilize lipid penetration. Notably, the same W217A substitution was previously shown to suppress GLIC function, and was considered the most impactful of several aromatic residues on the transmembrane surface [38]. Interestingly, a lack of double bonds in the intercalating tail was associated with the lipid head group interacting more closely with the protein surface, indicating a possible role for saturation in overall lipid-binding modes (Fig. 3). The relevance of lipid intercalation and saturation has been difficult to establish on the basis of structural data, given that resolved lipid tails are often limited to a few hydrocarbons beyond the glycerol group. An important extension of this work may be to apply similar analyses to simulations of mixed-lipid systems, albeit at substantially higher computational cost.

Lipid interactions in the outer leaflet were more variable, both between functional states and experimental methods, possibly reflecting larger conformational changes of the protein in this region. At the complementary-face site - one of the most consistently documented in previous X-ray structures - simulations indicated that lipid tails could penetrate deeper into the helical bundle upon channel opening (Fig. 5B), and even further in a state associated with desensitization. Interestingly, buried portions of this site have been shown to host allosteric modulators such as propofol, substituting for lipid-tail interactions [32]. State dependence was also suggested at the principal-face site, where the lipid head preferred a pose tilted in towards M3 in the closed state, but tilted out towards M4 in the open state. However, our closed cryo-EM structure was more consistent with open-state simulations, and with a detergent built in an open X-ray structure [16].

Indeed, the outward orientation was also sampled in closed-state simulations, albeit with lower frequency. The relevance of the inward-facing pose, possibly in the context of an alternative lipid head group, remains to be determined. The most provocative indication of state dependence was at the outer subunit interface, which did not contain strong density in either cryo-EM or simulations data for the closed state (Fig. 5A). In contrast, lipid occupancy at this site was evident in open simulations (Fig. 5B), including state-dependent contacts with P250, a conserved M2–M3 residue implicated in channel gating [39]. Although lipids have yet to be resolved at this intersubunit site in GLIC, they have been reported in open-state structures of both ELIC [40] and GluCl [41], and in a desensitized neuronal GABA(A) receptor [11].

This work demonstrates the combined power of cryo-EM and MD simulations to characterize membrane-protein lipid interactions. In leveraging extensive MD simulations to build lipids for the first time into a closed-state structure of GLIC, we were also able to capture features of lipid-tail saturation and potential state dependence that were not available from structural data alone. Knowledge of such interactions may prove useful in the development of lipid-like drugs or lipid-focused treatments of diseases related to malfunction of pLGICs.

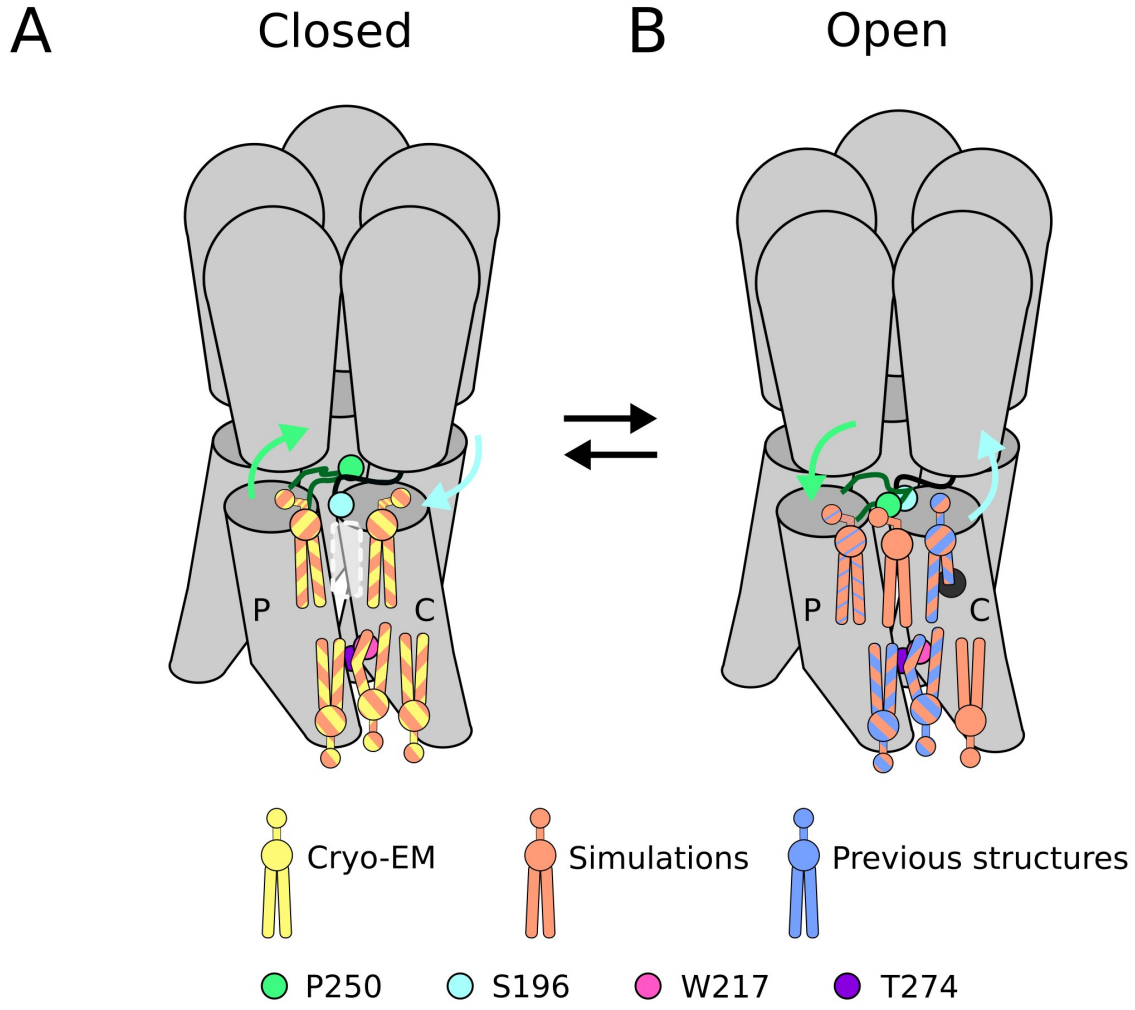

Figure 5: Lipid sites identified by cryo-EM and simulations. (A) In the closed state, five lipid interaction sites were independently identified through both cryo-EM and simulations. In the outer leaflet, two intrasubunit sites are situated at the principal (P) and complementary (C) subunits, with the lipid at the principal subunit site interacting with S196 of the pre-M1 loop. Particularly, no lipid site could be found at the subunit interface. In the inner leaflet, a buried lipid pose was found at the subunit interface, determined by interactions with T274 and W217 of the M3 and M1 helices, respectively. (B) In the open state, six lipid interaction sites were identified from simulations, out of which three sites were known from previous structures and one presumably occupied by a detergent molecule [16] (thin blue stripes). In the outer leaflet, an additional lipid site could be found at the subunit interface in the open state, interacting with P250 on the M2-M3 loop. Additionally, the site at the principal intrasubunit site is slighty closer to the M4 helix compared to the closed state, and the lipid site at the principal intrasubunit site has an increased likelihood of tail penetration into an allosteric pocket compared to the closed state. Lipid sites in the inner leaflet are at positions equivalent to those in the closed state.

Materials and methods

Molecular dynamics simulations and analysis

We analyzed previously published MSMs of GLIC gating under both resting and activating conditions [24]. In order to sample lipid movement more extensively, each of the 100 simulations was extended to 1.7 µs, resulting in an additional 50 µs sampling compared to [24]. For state classification, the additional simulation frames were projected onto the MSMs trained on the previously published simulations.

Time-based measures of protein-lipid interactions, such as the mean duration time and the exchange of interactions, were calculated for the 100×1.7 µs-long simulations using prolintpy [42] with a 4 Å interaction cutoff.

In order to investigate state-dependent protein-lipid interactions, all trajectory frames were classified according to the five clusters in [24], resulting in 19555 and 21941 frames for the closed and open protonated states, respectively, and 20632 and 13452 frames for the closed and open deprotonated states, respectively. Occupied densities were calculated from the frames corresponding to each cluster using VMD's volmap tool [43] for a selection of all whole lipids within 3 Å of the protein surface. In order to get representative snapshots of the protein-lipid interactions, we calculated global correlations between the computational densities and the selection of lipids used to derive the same densities using GROmaps [44], and extracted the 100 frames with the highest correlations. To ensure that all frames would not originate from a single trajectory, a maximum of 40% of the highest-correlating frames were allowed to originate from a single trajectory.

In order to explore the effect of mutations, we ran sets of 8×1.7 µs simulations on open wild-type GLIC (PDB ID: 4HFI) [45] with the modification W217A, T274A, or T274W. Each mutated protein was independently embedded in a POPC lipid bilayer, solvated by water and 0.1 M NaCl. Acidic residues (E26, E35, E67, E75, E82, D86, D88, E177, E243; H277 doubly protonated) were protonated to approximate the probable pattern at pH 4.6, as previously described [24, 30]. Constant pressure and temperature relaxation was carried out in four steps, restraining all heavy atoms in the first cycle, then only backbone atoms, then Cα atoms, and finally the M2 helices, for a total of 76 ns. Equilibration and production runs were performed using the Amber99SB-ILDN force field with Berger lipids [46], together with the TIP3P water model. Temperature coupling was achieved with velocity rescaling [47] and pressure coupling with the Parrinello-Rahman barostat [48]. Open-state mutagenesis simulations were prepared and run with GROMACS versions 2018.4 and 2020.5 [49]. Simulations extended from those described in [24] were prepared in a similar way as described above, but were prepared and run with GROMACS versions 2018.4 and 2019.3.

Conformational analysis and visualization of protein and lipids were performed with MDAnalysis [50, 51], PyEMMA 2.5.7 [52], and VMD [43].

Cryo-EM sample preparation and data acquisition

Experiments used in this project were previously reported in [26]. Briefly, C43(DE3) *E. coli* transformed with GLIC-MBP in vector pET-20b were cultured overnight at 37° C. Cells were then inoculated 1:100 into the 2xYT media containing 100 µg/mL ampicillin and grown at 37° C until they reached $OD_{600} = 0.7$. Next, the cells were induced with 100 µM isopropyl-β-D-1-thiogalactopyranoside (IPTG), and shaken overnight at 20° C. Membranes were harvested from cell pellets by sonication and ultracentrifugation in buffer A (300 mM NaCl, 20 mM Tris-HCl pH 7.4) supplemented with 1 mg/mL lysozyme, 20 µg/mL DNase I, 5 mM $MgCl_2$, and protease inhibitors. At this point the cells were either frozen or immediately solubilized in 2% n-dodecyl-β-D-maltoside (DDM). Amylose affinity resin (NEB) was used for purification of fusion protein in batch which was eluted in buffer B (buffer A with 0.02% DDM) with 2–20 mM maltose followed by size exclusion chromatography in buffer B. After overnight thrombin digestion, GLIC was isolated from its fusion partner by size exclusion, and concentrated to 3–5 mg/mL by centrifugation.

Quantifoil 1.2/1.3 Cu 300 mesh grids (Quantifoil Micro Tools) were used for sample preparation. The grids were glow-discharged in methanol vapor directly before 3 µl of sample was applied to them. Following a 1.5 s blot they were plunge-frozen into liquid ethane using a FEI Vitrobot Mark IV. Movies were collected on an FEI Titan Krios 300 kV microscope with a K2-Summit direct electron detector camera at nominal 165,000x magnification, equivalent to a pixel spacing of 0.82Å. A total dose of 40.8 $e^-/Å^2$ was used to collect 40 frames over 6 sec, with defocus values ranging from -2.0 to -3.8 µm.

Image processing and model building

Processing was performed through the RELION 4.0-beta-2 pipeline [53]. Motion correction was performed with Relion's own implementation [54], followed by a defocus estimation from the motion corrected micrographs using CtfFind4 [55]. Following manual picking, initial 2D classification was performed to generate references for autopicking. Particles were extracted after autopicking and binned, followed by a 2D classification of entire dataset. A smaller subset of particles was used to generate an Initial model, which was used in a consecutive 3D auto-refinement. The acquired alignment parameters were used to identify and remove noisy particles through multiple rounds of pre-aligned 2D- and 3D-classification. The final set of particles was then refined, using the best 3D reconstruction as reference. Particle polishing and per-particle CTF parameters were estimated from the resulting reconstruction using RELION 4.0-beta-2. Global beam-tilt was estimated from the micrographs and correction applied. Micelle density was subtracted and the final 3D auto-refinement was performed using a soft mask covering the protein, followed by post-processing. Local resolution was estimated using the RELION implementation. Autosharpen map tool in PHENIX 1.19.2-4158 [56] was used to improve the visibility of peripheral lipid and detergent densities around the protein.

The model was built from a template cryo-EM structure determined at pH 7 (PDB ID: 6ZGD [26]), fitted to the reconstructed density. PHENIX 1.19.2-4158 real-space refinement was used to refine the model, imposing 5-fold symmetry through NCS restraints detected from the reconstructed cryo-EM map. The model was incrementally adjusted in COOT 0.9.6 EL [57] and re-refined until conventional quality metrics were optimized in agreement with the reconstruction. Model statistics are summarized in Table 1. Lipids were built by importing a canonical SMILES format of POPC[58] into COOT and adjusted into the cryo-EM density in each site individually.

Molecular visualizations were created with VMD [43] and ChimeraX [59].

Data Availability

Cryo-EM density maps of the pentameric ligand-gated ion channel GLIC in detergent micelles have been deposited in the Electron Microscopy Data Bank under accession number EMD-15649. The deposition includes the cryo-EM sharpened and unsharpened maps, both half-maps and the mask used for final FSC calculation. Coordinates of the model have been deposited in the Protein Data Bank. The accession numbers for the structure is 8ATG. State-clustered simulations frames, computational lipid densities, parameter files, and full trajectories of mutant simulations can be accessed at https://doi.org/10.5281/zenodo.7058272.

Acknowledgments

The authors would like to thank the Swedish Cryo-EM National Facility staff, especially Marta Carroni and Stefan Fleischmann from Stockholm and Michael Hall from Umeå, for kind assistance with data collection. This work was supported by the Knut and Alice Wallenberg Foundation, and the Swedish Research Council (2019-04433, 2021-05806), the Swedish e-Science Research Centre (SeRC), the BioExcel Center of Excellence (EU-823830), and the Sven and Lily Lawskis Fond (UR). Cryo-EM data were collected at the Swedish national cryo-EM facility funded by the Knut and Alice Wallenberg Foundation, Erling Persson and Kempe Foundations. Computational resources were provided by the Swedish National Infrastructure for Computing (SNIC).

Author Contributions

Conceptualisation: CB, UR; Methodology: CB, UR; Investigation: CB, UR; data curation: CB, UR; Writing - original draft: CB, UR, RJH; Writing - review and editing: CB, UR, RJH, EL; Funding acquisition: EL; Supervision: RJH, EL.

Competing interests

The authors declare no conflicts of interest.

References

[1] Asba Tasneem, Lakshminarayan M Iyer, Eric Jakobsson, and L Aravind. Identification of the prokaryotic ligand-gated ion channels and their implications for the mechanisms and origins of animal cys-loop ion channels. *Genome biology*, 6(1):1–12, 2005.

[2] Anna L Duncan, Wanling Song, and Mark SP Sansom. Lipid-dependent regulation of ion channels and g protein–coupled receptors: insights from structures and simulations. *Annual Review of Pharmacology and Toxicology*, 60:31–50, 2020.

[3] Jean-Luc Popot, Jean Cartaud, and Jean-Pierre Changeux. Reconstitution of a functional acetylcholine receptor. *European Journal of Biochemistry*, 118(2):203–214, 1981.

[4] M. Criado, H. Eibl, and F. J. Barrantes. Effects of lipids on acetylcholine receptor. essential need of cholesterol for maintenance of agonist-induced state transitions in lipid vesicles. *Biochemistry*, 21(15):3622–3629, Jul 1982.

[5] Tung Ming Fong and Mark G. McNamee. Correlation between acetylcholine receptor function and structural properties of membranes. *Biochemistry*, 25(4):830–840, Feb 1986.

[6] Corrie J.B. daCosta, Andrei A. Ogrel, Elizabeth A. McCardy, Michael P. Blanton, and John E. Baenziger. Lipid-protein interactions at the nicotinic acetylcholine receptor: A functional coupling between nicotinic receptors and phosphatidic acid-containing lipid bilayers*. *Journal of Biological Chemistry*, 277(1):201–208, 2002.

[7] Mackenzie J. Thompson and John E. Baenziger. Structural basis for the modulation of pentameric ligand-gated ion channel function by lipids. *Biochimica et Biophysica Acta (BBA) - Biomembranes*, 1862(9):183304, 2020.

[8] José A Poveda, A Marcela Giudici, M Lourdes Renart, Andrés Morales, and José M González-Ros. Towards understanding the molecular basis of ion channel modulation by lipids: Mechanistic models and current paradigms. *Biochimica Et Biophysica Acta (BBA)-Biomembranes*, 1859(9):1507–1516, 2017.

[9] Shaotong Zhu, Colleen M Noviello, Jinfeng Teng, Richard M Walsh, Jeong Joo Kim, and Ryan E Hibbs. Structure of a human synaptic gabaa receptor. *Nature*, 559(7712):67–72, 2018.

[10] Simonas Masiulis, Rooma Desai, Tomasz Uchański, Itziar Serna Martin, Duncan Laverty, Dimple Karia, Tomas Malinauskas, Jasenko Zivanov, Els Pardon, Abhay Kotecha, et al. Gabaa receptor signalling mechanisms revealed by structural pharmacology. *Nature*, 565(7740):454–459, 2019.

[11] Duncan Laverty, Rooma Desai, Tomasz Uchański, Simonas Masiulis, Wojciech J Stec, Tomas Malinauskas, Jasenko Zivanov, Els Pardon, Jan Steyaert, Keith W Miller, et al. Cryo-em structure of the human $\alpha1\beta3\gamma2$ gabaa receptor in a lipid bilayer. *Nature*, 565(7740):516–520, 2019.

[12] Richard M Walsh, Soung-Hun Roh, Anant Gharpure, Claudio L Morales-Perez, Jinfeng Teng, and Ryan E Hibbs. Structural principles of distinct assemblies of the human $\alpha4\beta2$ nicotinic receptor. *Nature*, 557(7704):261–265, 2018.

[13] Anant Gharpure, Jinfeng Teng, Yuxuan Zhuang, Colleen M Noviello, Richard M Walsh Jr, Rico Cabuco, Rebecca J Howard, Nurulain T Zaveri, Erik Lindahl, and Ryan E Hibbs. Agonist selectivity and ion permeation in the $\alpha3\beta4$ ganglionic nicotinic receptor. *Neuron*, 104(3):501–511, 2019.

[14] Md Mahfuzur Rahman, Jinfeng Teng, Brady T Worrell, Colleen M Noviello, Myeongseon Lee, Arthur Karlin, Michael HB Stowell, and Ryan E Hibbs. Structure of the native muscle-type nicotinic receptor and inhibition by snake venom toxins. *Neuron*, 106(6):952–962, 2020.

[15] Yue Zhao, Sanling Liu, Yingxin Zhou, Mengge Zhang, Haopeng Chen, H Eric Xu, Demeng Sun, Lei Liu, and Changlin Tian. Structural basis of human $\alpha 7$ nicotinic acetylcholine receptor activation. *Cell research*, 31(6):713–716, 2021.

[16] Haidai Hu, Kenichi Ataka, Anaïs Menny, Zaineb Fourati, Ludovic Sauguet, Pierre-Jean Corringer, Patrice Koehl, Joachim Heberle, and Marc Delarue. Electrostatics, proton sensor, and networks governing the gating transition in glic, a proton-gated pentameric ion channel. *Proceedings of the National Academy of Sciences*, 115(52):E12172–E12181, 2018.

[17] Ludovic Sauguet, Azadeh Shahsavar, Frédéric Poitevin, Christèle Huon, Anaïs Menny, Àkos Nemecz, Ahmed Haouz, Jean-Pierre Changeux, Pierre-Jean Corringer, and Marc Delarue. Crystal structures of a pentameric ligand-gated ion channel provide a mechanism for activation. *Proceedings of the National Academy of Sciences*, 111(3):966–971, 2014.

[18] Jeong Joo Kim and Ryan E. Hibbs. Direct structural insights into gabaa receptor pharmacology. *Trends in Biochemical Sciences*, 46(6):502–517, 2021.

[19] Akshay Sridhar, Sarah C.R. Lummis, Diletta Pasini, Aujan Mehregan, Marijke Brams, Kumiko Kambara, Daniel Bertrand, Erik Lindahl, Rebecca J. Howard, and Chris Ulens. Regulation of a pentameric ligand-gated ion channel by a semiconserved cationic lipid-binding site. *Journal of Biological Chemistry*, 297(2), Aug 2021.

[20] Noah M Dietzen, Mark J Arcario, Lawrence J Chen, II Petroff, John T, K Trent Moreland, Kathiresan Krishnan, Grace Brannigan, Douglas F Covey, and Wayland WL Cheng. Polyunsaturated fatty acids inhibit a pentameric ligand-gated ion channel through one of two binding sites. *eLife*, 11:e74306, jan 2022.

[21] Liam Sharp and Grace Brannigan. Spontaneous lipid binding to the nicotinic acetylcholine receptor in a native membrane. *The Journal of Chemical Physics*, 154(18):185102, 2021.

[22] Marc A. Dämgen and Philip C. Biggin. State-dependent protein-lipid interactions of a pentameric ligand-gated ion channel in a neuronal membrane. *PLOS Computational Biology*, 17(2):1–24, 02 2021.

[23] Alessandro Crnjar and Carla Molteni. Cholesterol content in the membrane promotes key lipid-protein interactions in a pentameric serotonin-gated ion channel. *Biointerphases*, 15(6):061018, 2020.

[24] Cathrine Bergh, Stephanie A Heusser, Rebecca Howard, and Erik Lindahl. Markov state models of proton- and pore-dependent activation in a pentameric ligand-gated ion channel. *eLife*, 10:e68369, oct 2021.

[25] Urška Rovšnik, Yuxuan Zhuang, Björn O Forsberg, Marta Carroni, Linnea Yvonnesdotter, Rebecca J Howard, and Erik Lindahl. Dynamic closed states of a ligand-gated ion channel captured by cryo-em and simulations. *Life Science Alliance*, 4(8), 2021.

[26] Urška Rovšnik, Yuxuan Zhuang, Björn O Forsberg, Marta Carroni, Linnea Yvonnesdotter, Rebecca J Howard, and Erik Lindahl. Dynamic closed states of a ligand-gated ion channel captured by cryo-em and simulations. *Life Science Alliance*, 4(8), 2021.

[27] Thomas C Terwilliger, Steven J Ludtke, Randy J Read, Paul D Adams, and Pavel V Afonine. Improvement of cryo-em maps by density modification. *Nature methods*, 17(9):923–927, 2020.

[28] Arjen J Jakobi, Matthias Wilmanns, and Carsten Sachse. Model-based local density sharpening of cryo-em maps. *Elife*, 6:e27131, 2017.

[29] Nicolas Bocquet, Hugues Nury, Marc Baaden, Chantal Le Poupon, Jean-Pierre Changeux, Marc Delarue, and Pierre-Jean Corringer. X-ray structure of a pentameric ligand-gated ion channel in an apparently open conformation. *Nature*, 457(7225):111–114, 2009.

[30] Hugues Nury, Catherine Van Renterghem, Yun Weng, Alphonso Tran, Marc Baaden, Virginie Dufresne, Jean-Pierre Changeux, James M. Sonner, Marc Delarue, and Pierre-Jean Corringer. X-ray structures of general anaesthetics bound to a pentameric ligand-gated ion channel. *Nature*, 469(7330):428–431, Jan 2011.

[31] Sandip Basak, Nicolaus Schmandt, Yvonne Gicheru, and Sudha Chakrapani. Crystal structure and dynamics of a lipid-induced potential desensitized-state of a pentameric ligand-gated channel. *eLife*, 6:e23886, mar 2017.

[32] Stephanie A. Heusser, Marie Lycksell, Xueqing Wang, Sarah E. McComas, Rebecca J. Howard, and Erik Lindahl. Allosteric potentiation of a ligand-gated ion channel is mediated by access to a deep membrane-facing cavity. *Proceedings of the National Academy of Sciences*, 115(42):10672–10677, 2018.

[33] Rob Phillips, Tristan Ursell, Paul Wiggins, and Pierre Sens. Emerging roles for lipids in shaping membrane-protein function. *Nature*, 459(7245):379–385, 2009.

[34] Julio F Cordero-Morales and Valeria Vásquez. How lipids contribute to ion channel function, a fat perspective on direct and indirect interactions. *Current opinion in structural biology*, 51:92–98, 2018.

[35] Ilya Levental and Ed Lyman. Regulation of membrane protein structure and function by their lipid nano-environment. *Nature Reviews Molecular Cell Biology*, Sep 2022.

[36] Christos Lamprakis, Ioannis Andreadelis, John Manchester, Camilo Velez-Vega, José S. Duca, and Zoe Cournia. Evaluating the efficiency of the martini force field to study protein dimerization in aqueous and membrane environments. *Journal of Chemical Theory and Computation*, 17(5):3088–3102, May 2021.

[37] Casey L. Carswell, Jiayin Sun, and John E. Baenziger. Intramembrane aromatic interactions influence the lipid sensitivities of pentameric ligand-gated ion channels *. *Journal of Biological Chemistry*, 290(4):2496–2507, Jan 2015.

[38] J. P. Daniel Therien and John E. Baenziger. Pentameric ligand-gated ion channels exhibit distinct transmembrane domain archetypes for folding/expression and function. *Scientific Reports*, 7(1):450, Mar 2017.

[39] Przemyslaw T Kaczor, Michał A Michałowski, and Jerzy W Mozrzymas. α1 proline 277 residues regulate gabaar gating through m2-m3 loop interaction in the interface region. *ACS Chemical Neuroscience*, 2022.

[40] John T Petroff, Noah M Dietzen, Ezry Santiago-McRae, Brett Deng, Maya S Washington, Lawrence J Chen, K Trent Moreland, Zengqin Deng, Michael Rau, James AJ Fitzpatrick, et al. Open-channel structure of a pentameric ligand-gated ion channel reveals a mechanism of leaflet-specific phospholipid modulation. *Nature Communications*, 13(1):1–16, 2022.

[41] Thorsten Althoff, Ryan E Hibbs, Surajit Banerjee, and Eric Gouaux. X-ray structures of glucl in apo states reveal a gating mechanism of cys-loop receptors. *Nature*, 512(7514):333–337, 2014.

[42] Besian I Sejdiu and D Peter Tieleman. ProLint: a web-based framework for the automated data analysis and visualization of lipid–protein interactions. *Nucleic Acids Research*, 05 2021. gkab409.

[43] William Humphrey, Andrew Dalke, and Klaus Schulten. VMD – Visual Molecular Dynamics. *Journal of Molecular Graphics*, 14:33–38, 1996.

[44] Rodolfo Briones, Christian Blau, Carsten Kutzner, Bert L. de Groot, and Camilo Aponte-Santamaría. Gromaps: A gromacs-based toolset to analyze density maps derived from molecular dynamics simulations. *Biophysical Journal*, 116(1):4–11, 2019.

[45] Ludovic Sauguet, Frédéric Poitevin, Samuel Murail, Catherine Van Renterghem, Gustavo Moraga-Cid, Laurie Malherbe, Andrew W Thompson, Patrice Koehl, Pierre-Jean Corringer, Marc Baaden, and Marc Delarue. Structural basis for ion permeation mechanism in pentameric ligand-gated ion channels. *The EMBO Journal*, 32(5):728–741, 2013.

[46] O. Berger, O. Edholm, and F. Jähnig. Molecular dynamics simulations of a fluid bilayer of dipalmitoylphosphatidylcholine at full hydration, constant pressure, and constant temperature. *Biophysical Journal*, 72(5):2002–2013, 1997.

[47] Giovanni Bussi, Davide Donadio, and Michele Parrinello. Canonical sampling through velocity rescaling. *The Journal of Chemical Physics*, 126(1):014101, 2007.

[48] M. Parrinello and A. Rahman. Polymorphic transitions in single crystals: A new molecular dynamics method. *Journal of Applied Physics*, 52(12):7182–7190, 1981.

[49] Mark James Abraham, Teemu Murtola, Roland Schulz, Szilárd Páll, Jeremy C. Smith, Berk Hess, and Erik Lindahl. Gromacs: High performance molecular simulations through multi-level parallelism from laptops to supercomputers. *SoftwareX*, 1-2:19 – 25, 2015.

[50] Naveen Michaud-Agrawal, Elizabeth J. Denning, Thomas B. Woolf, and Oliver Beckstein. Mdanalysis: A toolkit for the analysis of molecular dynamics simulations. *Journal of Computational Chemistry*, 32(10):2319–2327, 2011.

[51] Richard J. Gowers, Max Linke, Jonathan Barnoud, Tyler J. E. Reddy, Manuel N. Melo, Sean L. Seyler, Jan Domański, David L. Dotson, Sébastien Buchoux, Ian M. Kenney, and Oliver Beckstein. MDAnalysis: A Python Package for the Rapid Analysis of Molecular Dynamics Simulations. In Sebastian Benthall and Scott Rostrup, editors, *Proceedings of the 15th Python in Science Conference*, pages 98 – 105, 2016.

[52] Martin K. Scherer, Benjamin Trendelkamp-Schroer, Fabian Paul, Guillermo Pérez-Hernández, Moritz Hoffmann, Nuria Plattner, Christoph Wehmeyer, Jan-Hendrik Prinz, and Frank Noé. PyEMMA 2: A Software Package for Estimation, Validation, and Analysis of Markov Models. *Journal of Chemical Theory and Computation*, 11:5525–5542, October 2015.

[53] Dari Kimanius, Liyi Dong, Grigory Sharov, Takanori Nakane, and Sjors HW Scheres. New tools for automated cryo-em single-particle analysis in relion-4.0. *Biochemical Journal*, 478(24):4169–4185, 2021.

[54] Jasenko Zivanov, Takanori Nakane, and Sjors HW Scheres. A bayesian approach to beam-induced motion correction in cryo-em single-particle analysis. *IUCrJ*, 6(1):5–17, 2019.

[55] Alexis Rohou and Nikolaus Grigorieff. Ctffind4: Fast and accurate defocus estimation from electron micrographs. *Journal of structural biology*, 192(2):216–221, 2015.

[56] Paul D Adams, Pavel V Afonine, Gábor Bunkóczi, Vincent B Chen, Ian W Davis, Nathaniel Echols, Jeffrey J Headd, L-W Hung, Gary J Kapral, Ralf W Grosse-Kunstleve, et al. Phenix: a comprehensive python-based system for macromolecular structure solution. *Acta Crystallographica Section D: Biological Crystallography*, 66(2):213–221, 2010.

[57] Paul Emsley and Kevin Cowtan. Coot: model-building tools for molecular graphics. *Acta crystallographica section D: biological crystallography*, 60(12):2126–2132, 2004.

[58] Sunghwan Kim, Jie Chen, Tiejun Cheng, Asta Gindulyte, Jia He, Siqian He, Qingliang Li, Benjamin A Shoemaker, Paul A Thiessen, Bo Yu, et al. Pubchem in 2021: new data content and improved web interfaces. *Nucleic acids research*, 49(D1):D1388–D1395, 2021.

[59] Thomas D Goddard, Conrad C Huang, Elaine C Meng, Eric F Pettersen, Gregory S Couch, John H Morris, and Thomas E Ferrin. Ucsf chimerax: Meeting modern challenges in visualization and analysis. *Protein Science*, 27(1):14–25, 2018.

Supplementary information

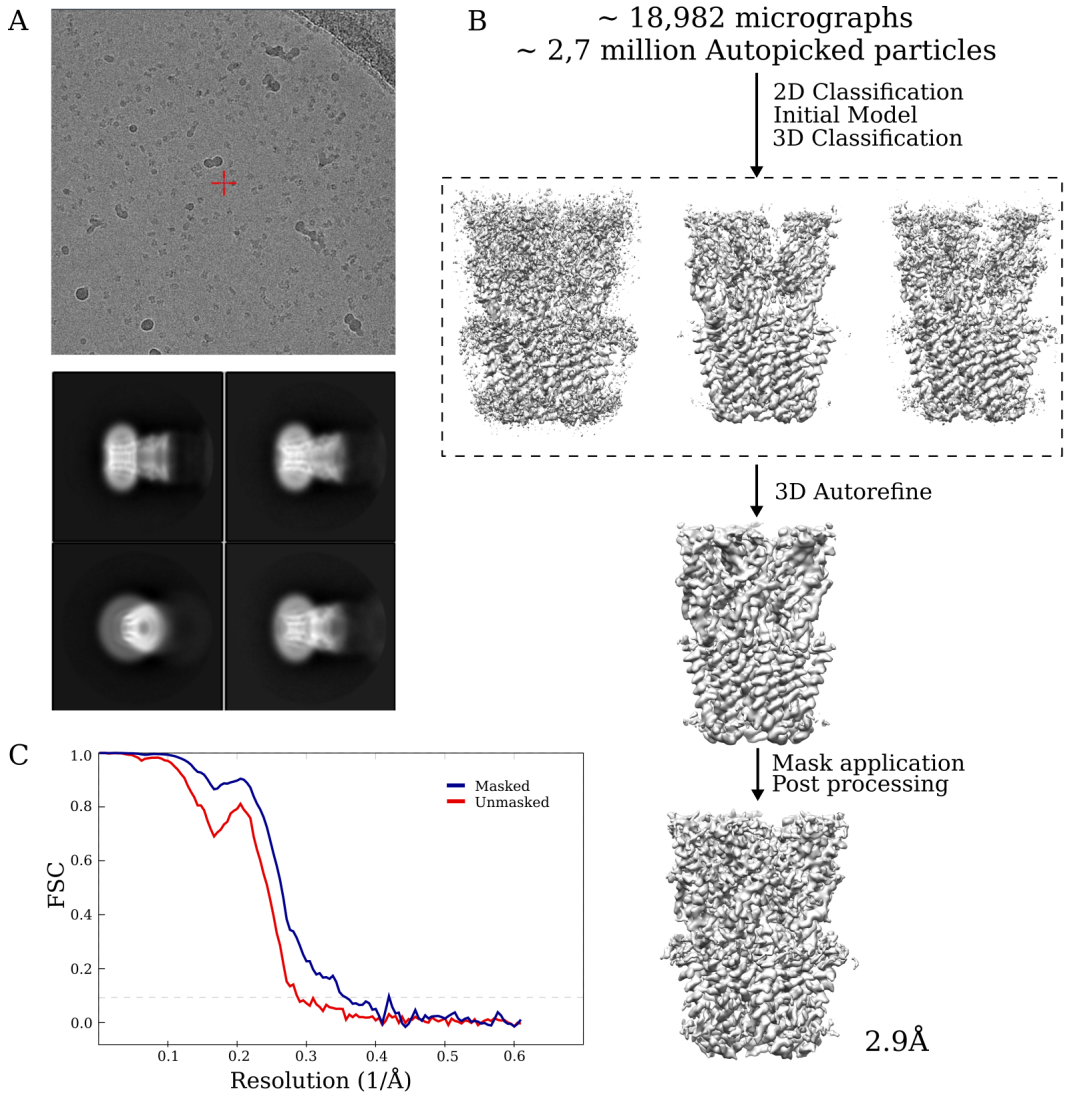

Figure S1: Cryo-EM data and processing pipeline. (A) Representative micrograph from a dataset collected on a Titan Krios, showing detergent-solubilized GLIC particles (*top*. Representative 2D class averages at 0.82 Å/px in a 256 x 256 pixel box and a 180 Å mask *bottom*. (B) Overview of the cryo-EM processing pipeline for a merged GLIC data. (C) FSC curves for unmasked (*red*) and masked (*blue*) map.

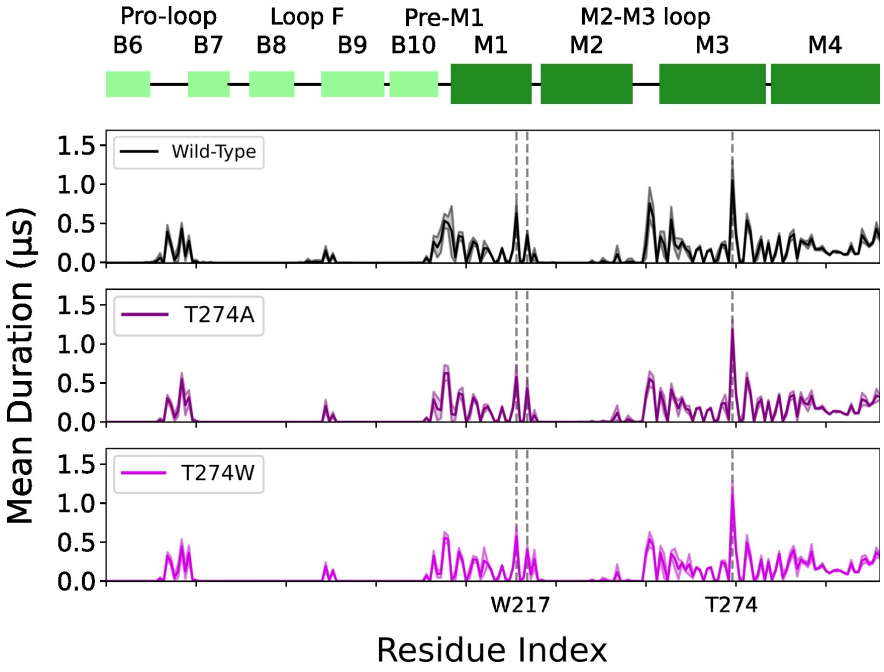

Figure S2: W217 and T274 mutants mean duration times compared to wild type. Mean duration time (μs) of lipid interaction time for GLIC wild type (black, *top row*), T274A mutant (purple, *middle row*) and T274W mutant (light purple, *bottom row*).

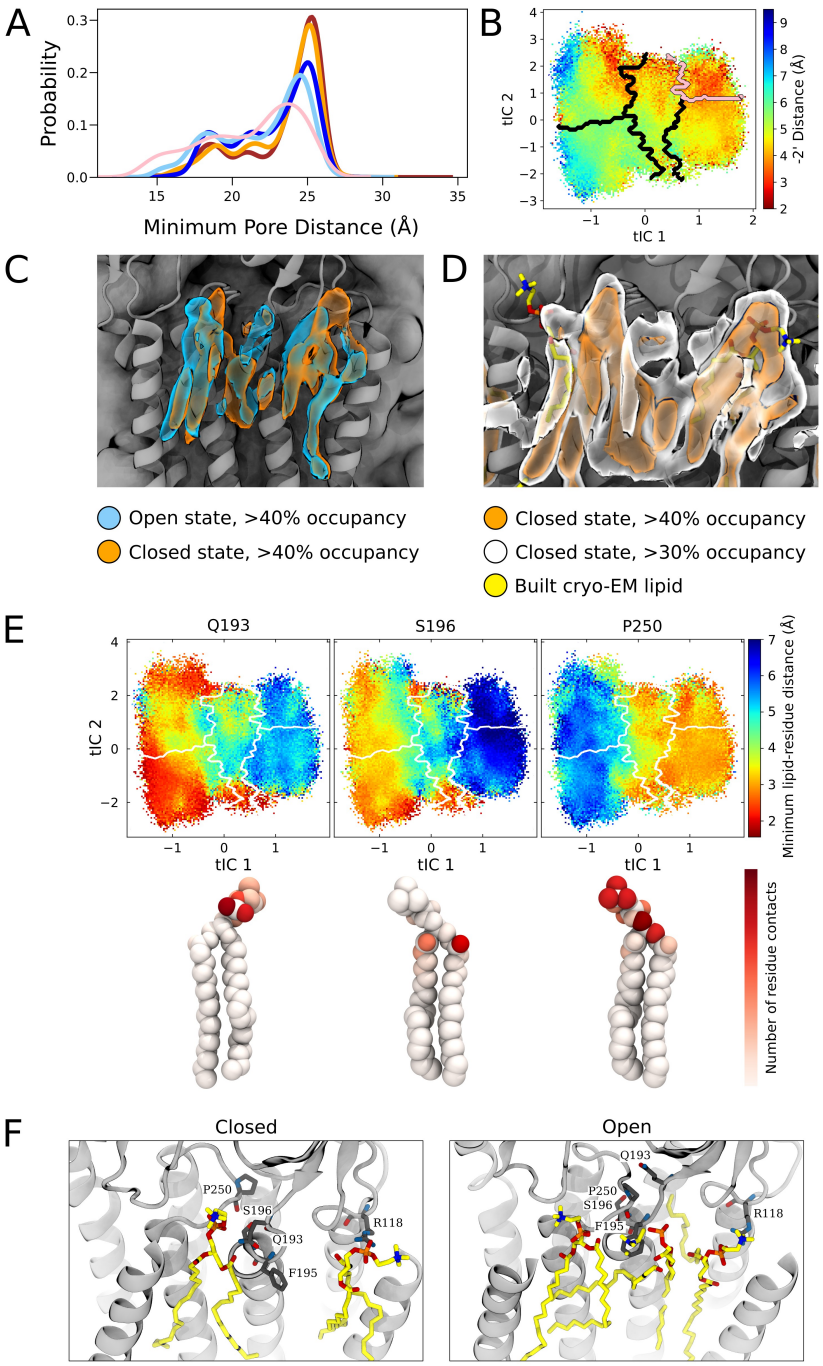

Figure S3: State-dependent lipid interactions and conformational changes in the upper transmembrane domain. (A) Radial distributions of nearest lipid atom from the upper pore, with a presumed pre-desensitized state displaying the highest probability of lipid tail penetration (pink), followed by open states (dark blue, light blue) and closed states (red, orange). (B) Radial distance to the -2' gate projected onto the tIC space at activating conditions. The presumed pre-desensitized state is marked in pink. (C) Lipid densities derived from simulations with ≥40% occupancies, representing open (blue) and closed (orange) states. (D) Lipid densities from closed state simulation frames with ≥40% occupancy (orange) and ≥30% (white). Built cryo-EM lipids are shown in yellow. (E) Minimum residue-lipid distance projected onto the activating condition free energy landscape for residues Q193, S196 and P250. (F) The normalized number of residue-lipid atom contacts displayed for each of the residues in (E), with red areas highlighting atoms with close interactions to the residue in (E). (G) Representative GLIC open and closed state simulation frames with the highest correlations between lipid positions and the computational occupancies (Figure 4B).

Table 1: Cryo-EM data collection and model refinement statistics

Data Collection	
Microscope	FEI Titan Krios
Magnification	165,000
Voltage (kV)	300
Electron exposure ($e^-/Å^2$)	~ 40
Defocus Range (µm)	-2.6 – -3.8
Pixel Size (Å)	0.82
Symmetry Imposed	C5
Number of Images	~ 18982
Particles Picked	$\sim 2,7$ mil
Particles Refined	16,586
Refinement	
Resolution (Å)	2.9
FSC Threshold	0.143
Map sharpening B-factor	-80
Model Composition	
Non-hydrogen Protein atoms	12,010
Protein Residues	1555
Ligands	0
B-factor ($Å^{2)}$	144
RMSD	
Bond Lengths (Å)	0.004
Bond Angles (°)	0.584
Validation	
Molprobity Score	1.84
Clashscore	6.82
Poor Rotamers (%)	0
Ramachandran Plot	
Favored (%)	92.6
Allowed (%)	7.4
Outliers (%)	0